Intracellular Ca^{2+} regulation of H^+/Ca^{2+} antiporter YfkE mediated by a Ca^{2+} mini-sensor

Shuo Lu[a], Zhenlong Li[b], Alemayehu A. Gorfe[b], and Lei Zheng[a,1]

[a]Department of Biochemistry and Molecular Biology, Center for Membrane Biology, The University of Texas Health Science Center at Houston McGovern Medical School, Houston, TX 77030; and [b]Department of Integrative Biology and Pharmacology, The University of Texas Health Science Center at Houston McGovern Medical School, Houston, TX 77030

Edited by Nieng Yan, Princeton University, Princeton, NJ, and approved March 19, 2020 (received for review October 23, 2019)

The H^+/Ca^{2+} (calcium ion) antiporter (CAX) plays an important role in maintaining cellular Ca^{2+} homeostasis in bacteria, yeast, and plants by promoting Ca^{2+} efflux across the cell membranes. However, how CAX facilitates Ca^{2+} balance in response to dynamic cytosolic Ca^{2+} perturbations is unknown. Here, we identified a type of Ca^{2+} "mini-sensor" in YfkE, a bacterial CAX homolog from *Bacillus subtilis.* The mini-sensor is formed by six tandem carboxylate residues within the transmembrane (TM)5-6 loop on the intracellular membrane surface. Ca^{2+} binding to the mini-sensor triggers the transition of the transport mode of YfkE from a high-affinity to a low-affinity state. Molecular dynamics simulation and fluorescence resonance energy transfer analysis suggest that Ca^{2+} binding to the mini-sensor causes an adjacent segment, namely, the exchanger inhibitory peptide (XIP), to move toward the Ca^{2+} translocation pathway to interact with TM2a in an inward-open cavity. The specific interaction was demonstrated with a synthetic peptide of the XIP, which inhibits YfkE transport and interrupts conformational changes mediated by the mini-sensor. By comparing the apo and Ca^{2+}-bound CAX structures, we propose the following Ca^{2+} transport regulatory mechanism of YfkE: Ca^{2+} binding to the mini-sensor induces allosteric conformational changes in the Ca^{2+} translocation pathway via the XIP, resulting in a rearrangement of the Ca^{2+}-binding transport site in the midmembrane. Since the Ca^{2+} mini-sensor and XIP sequences are also identified in other CAX homologs and/or Ca^{2+} transporters, including the mammalian Na^+/Ca^{2+} exchanger (NCX), our study provides a regulatory mechanism for the Ca^{2+}/cation transporter superfamily.

calcium ion | transporter | conformational changes | acidic motif | allosteric regulation

Ca^{2+} is an important messenger in both prokaryotic and eukaryotic cells, regulating numerous cellular processes including the cell cycle, development, gene expression, and metabolism (1, 2). Ca^{2+}-mediated signaling is triggered by Ca^{2+} influx through Ca^{2+} channels. To restore excited cells back to their resting state, excess Ca^{2+} is removed from the cytosol out of the cells by Ca^{2+}-ATPase and Ca^{2+}/cation antiporters (CaCA). CaCA proteins including CAXs and NCXs promote uphill Ca^{2+} efflux using a counter electrochemical gradient of H^+ or Na^+, playing essential roles in maintaining Ca^{2+} homeostasis (3).

CAXs are mainly found in fungi and plants where they are present in the plasma membrane and tonoplast (4, 5). In plants, CAXs transport cytosolic Ca^{2+} into acidic vacuoles, which is a key mediator for stress responses to various stimuli including cold, salinity, and soil pH (6–8). CAX homologs are also found ubiquitously in prokaryotes (3), although their physiological roles are poorly characterized. Given their specific Ca^{2+} transport activity (9, 10), bacterial CAX proteins may be involved in many bacterial Ca^{2+}-mediated events, such as sporulation, chemotaxis, swarming motility, and virulence (11).

CAXs are integral membrane proteins consisting of 11 TM helices. Recently, crystal structures of three CAX homologous proteins from bacteria and yeast have provided structural insights into the Ca^{2+} transport mechanism (12–14). These CAX structures exhibit similar protein architectures in which four helices (TMs 2, 3, 7, and 8) assemble a Ca^{2+} translocation pathway. TMs 2 and 7 are kinked toward each other in an X-shaped conformation. At the kink intersection, two conserved glutamate residues form a transport Ca^{2+}-binding site midway in the translocation pathway. Mutation of these two carboxylate residues abrogates the Ca^{2+} transport activity (12). These CAX structures exhibit inward-open conformations with a large cavity opening toward the cytoplasmic surface. Based on these structures, a Ca^{2+}/H^+ alternating access mechanism has been proposed in which substrate binding triggers protein conformational changes by rotating kinked TMs 2 and 7 to facilitate Ca^{2+} efflux across the membrane. This transport mechanism is supported by the structure of archaeal Na^+/Ca^{2+} exchanger (NCX_{mj}) (15). In contrast to the CAX structures, the structure of NCX_{mj} exhibits an outward-open conformation that is largely attributed to counterclockwise rotations of TMs 2a and 7b around the transport Ca^{2+}-binding site (12). Despite the wealth of structural information, the mechanism of substrate binding is still elusive since the apo structure of the bacterial CAX homolog YfkE from *B. subtilis,* determined by our group, and the Ca^{2+}-bound yeast vacuolar Ca^{2+}/H^+ exchanger (VCX1) structure both exhibit similar inward-open conformations, regardless of their distinct substrate-binding states (12, 13). Whether multiple states of substrate binding are involved in a Ca^{2+} transport cycle is unknown and requires further investigation.

Ca^{2+} signaling is not merely regulated by increases and decreases in cytosolic [Ca^{2+}], but it is also dependent on the specific rate, magnitude, frequency, and spatiotemporal patterns of

Significance

Ca^{2+} is essential for life, not only as a basic element, but also due to its versatile role in cellular signaling. H^+/Ca^{2+} antiporter CAX proteins facilitate cellular Ca^{2+} homeostasis in microorganisms, yeast, and plants by catalyzing Ca^{2+} extrusion from the cytosol driven by an inward H^+ gradient. In this paper, we reveal a self-regulatory mechanism of CAX. We found that CAX senses changes in cytosolic Ca^{2+} levels to adjust its Ca^{2+} transport activity. This regulation is mediated by a Ca^{2+} mini-sensor to alter the conformation of the Ca^{2+} translocation pathway. This regulatory mechanism is conserved in both prokaryotes and eukaryotes. Our study provides insights into the working mechanism of these important Ca^{2+} transporter proteins in the cell membrane.

Author contributions: S.L., Z.L., A.A.G., and L.Z. designed research; S.L., Z.L., A.A.G., and L.Z. performed research; S.L., Z.L., A.A.G., and L.Z. analyzed data; and A.A.G. and L.Z. wrote the paper.

The authors declare no competing interest.

This article is a PNAS Direct Submission.

[1]To whom correspondence may be addressed. Email: lei.zheng@uth.tmc.edu.

This article contains supporting information online at https://www.pnas.org/lookup/suppl/doi:10.1073/pnas.1918604117/-/DCSupplemental.

First published April 27, 2020.

the Ca^{2+} signal, the so called Ca^{2+} signature (1). This requires rapid response and tight control of Ca^{2+} transporters based on cytosolic Ca^{2+} levels. Mammalian NCX regulates its Ca^{2+} transport activity based on cytosolic $[Ca^{2+}]$ (16). This Ca^{2+} regulation is achieved by Ca^{2+} binding to the two tandem Ca^{2+}-binding domains (CBD1 and CBD2) of NCX within a large cytoplasmic loop of ∼500 amino acid residues between TMs 5 and 6 (17–19). However, those large CBD domains are only available in mammalian NCXs. In all CAX homologs, a short loop containing ∼30 amino acid residues is found at the analogous position (5). How CAXs fulfill their Ca^{2+} efflux functions in response to dynamic Ca^{2+} perturbations is still unclear.

Here, we reveal a regulatory mechanism of CAX. We found that YfkE is regulated by Ca^{2+} binding to its short intracellular TM5-6 loop. We identified a type of Ca^{2+} mini-sensor and an inhibitory peptide, XIP, within the loop. By using molecular dynamics (MD) simulation, fluorescence resonance energy transfer (FRET) and other biochemical approaches, we demonstrate how Ca^{2+} binding to the mini-sensor induces allosteric conformational changes via the XIP to alter the conformation of the Ca^{2+} translocation pathway. We anticipate that this Ca^{2+} regulatory mechanism is conserved in all CAX proteins. Since the XIP is also present in other Ca^{2+} transporter proteins including mammalian NCX, our study provides insights into the Ca^{2+} transport mechanism of the CaCA protein superfamily.

Results

YfkE catalyzes Ca^{2+} efflux using an inward H^+ gradient (9). Its transport activity was measured by detecting $^{45}Ca^{2+}$ influx into inside-out (ISO) vesicles. To eliminate Ca^{2+} from the cytosolic membrane surface, vesicles were treated with 1 mM ethylene glycol bis(β-aminoethyl ether)-*N*,*N*,*N*′,*N*′-tetraacetic acid (EGTA), and then free $[Ca^{2+}]_{cyto}$ in the reaction mixture was determined using a Ca^{2+}-EGTA calculator. Interestingly, the transport activity of YfkE exhibited biphasic kinetics (Fig. 1*A* and *SI Appendix*, Fig. S1) clearly demonstrated using Eadie–Hofstee plots (Fig. 1*B*). Data fitting indicated that YfkE transports Ca^{2+} with a high affinity ($K_m^H = 7 \pm 0.9$ μM, $V_m^H = 13.9 \pm 0.3$ μmol/min/mg) when $[Ca^{2+}]_{cyto}$ is low. When $[Ca^{2+}]_{cyto}$ increases, its substrate-binding affinity is significantly reduced by 25-fold, whereas V_{max} is increased by twofold ($K_m^L = 175.2 \pm 38.2$ μM, $V_{max}^L = 26.6 \pm 2.1$ μmol/min/mg). However, biphasic transport was only observed when using EGTA to strip any prebound Ca^{2+} from the ISO vesicle surface. Without EGTA treatment, YfkE showed single exponential Michalis–Menten kinetics and only exhibited the low-affinity transport state ($K_m = 220 \pm 24.5$ μM and $V_{max} = 34.4 \pm 6.3$ μmol/min/mg) (Fig. 1 *A* and *B*). These results suggest that Ca^{2+} binding to the intracellular membrane surface of YfkE regulates its Ca^{2+} transport activity.

In YfkE, the transport Ca^{2+}-binding site is embedded deeply in the midmembrane (12). Thus, we hypothesized that an additional Ca^{2+}-binding site is available on the intracellular protein surface, and this site contributes to the biphasic kinetics of YfkE. Despite the lack of large CBD domains, CAXs share a conserved acidic motif within the intracellular loop between TMs 5 and 6 (5) (Fig. 2 *A* and *B*). The acidic motif consists of tandem carboxylate residues. It was previously predicted to form a Ca^{2+}-binding site, although its role has not yet been characterized (4, 10); e.g., six tandem glutamate residues ($E^{194}EEEEPE^{200}$) are located within the TM5-6 loop in YfkE (Fig. 2*A*). We asked whether these carboxylate residues are involved in intracellular Ca^{2+} regulation of YfkE. When the residues Glu^{194}–Glu^{198} were substituted with five glycine residues ($YfkE^{5G}$), the transport assays indicated that $YfkE^{5G}$ remained active (Fig. 2*C*). However, the biphasic kinetics of YfkE was markedly changed. The transport activity of $YfkE^{5G}$ was proportionally linear as a function of $[Ca^{2+}]_{cyto}$, and no saturation was observed until ∼1 mM, regardless of EGTA treatment (Fig. 2*C*). We next examined Ca^{2+} binding to YfkE using isothermal titration calorimetry (ITC). The Ca^{2+} titration curve indicated that the Ca^{2+}-binding affinity (K_d) of $YfkE^{WT}$ is 9.7 ± 2.7 μM (Fig. 2*D*). In contrast, no specific Ca^{2+} binding was detected with the $YfkE^{5G}$ protein (Fig. 2*E*). Ca^{2+} binding to the acidic motif was directly confirmed using a synthetic peptide of the TM5-6 loop (Lys^{171}-Glu^{198}). Although Ca^{2+} titration to the peptide produced distinct endothermic changes, the ITC analysis yielded a K_d of 4.7 ± 0.9 μM, similar to that of the $YfkE^{WT}$ protein (Fig. 2*F*). No binding to other cations including Mg^{2+}, K^+, and Li^+ was detected (*SI Appendix*, Fig. S2 *A*, *C*, and *D*), while the peptide may interact with Cd^{2+}, a Ca^{2+} analog based on the ITC curves (*SI Appendix*, Fig. S2*B*). These results reveal that the small acidic motif forms a specific Ca^{2+}-binding site on the intracellular membrane surface, which may act as a Ca^{2+} mini-sensor to regulate the Ca^{2+} transport activity of YfkE.

To understand how the Ca^{2+} mini-sensor regulates YfkE transport, we have designed a FRET approach to monitor protein conformational changes within the TM5-6 loop (Fig. 3*A*). YfkE forms a homotrimer in the cell membrane and in detergent solutions (12). In each protomer, the residue Ala^{190} adjacent to the mini-sensor was mutated to cysteine (*SI Appendix*, Fig. S3*A*). The $YfkE^{A190C}$ protein was purified and labeled with a pair of thiol-reactive probes, Alexa Fluor 555 and 647. Protein conformational changes mediated by the Ca^{2+} mini-sensor were then detected by FRET between subunits within a YfkE trimer. Of note, mutation of A190C produced no change in YfkE transport activity (*SI Appendix*, Fig. S3*B*), and, therefore, its protein conformation likely represents that of wild type (WT). Fluorescence emission spectra

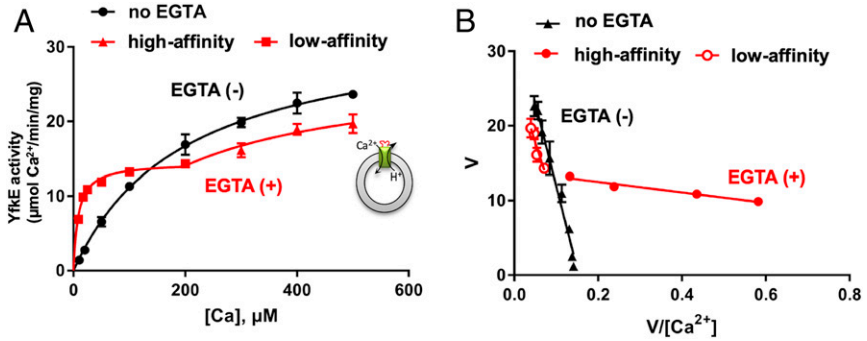

Fig. 1. Dual-state Ca^{2+} transport of YfkE. (*A*) $^{45}Ca^{2+}$ transport activity of YfkE measured using ISO vesicles, showing biphasic kinetics when vesicles were pretreated with 1 mM EGTA (red), and Michelis–Menton kinetics using vesicles without EGTA treatment (black). A cartoon model of the transport assay shows that YfkE (green bar) transport Ca^{2+} into the ISO vesicle (gray circles) using an outward H^+ gradient. (*B*) Eadie–Hofstee plots of data from *A*. Data fitting was carried out using the software Graphpad Prism 7. Error bars represent SDs from three independent experiments.

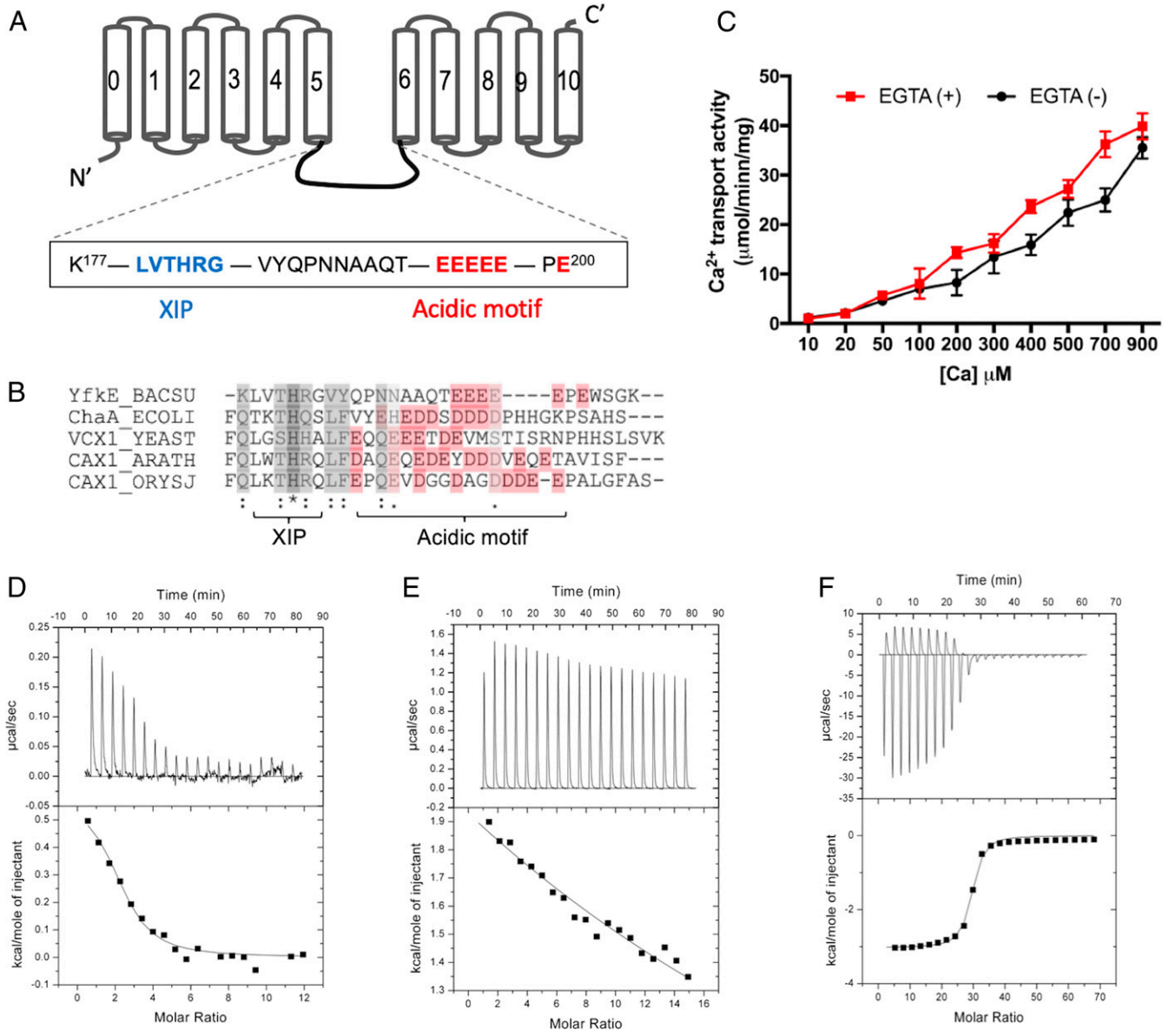

Fig. 2. Identification of Ca^{2+} mini-sensor in YfkE. (*A*) Topological model of YfkE with the sequences of the acidic motif (red) and XIP (blue) highlighted within the TM5-6 loop. (*B*) Sequence alignment of the TM5-6 loop of CAX homologs: YfkE from *B. subtilis* (yfkE_BACSU), ChaA from *Escherichia coli* (ChaA_ECOLI), VCX1 from *Saccharomyces cerevisiae* (VCX1_YEAST), CAX1 from *Arabidopsis thaliana* (CAX1_ARATH), and CAX1a from *Oryza sativa subsp. Japonica* (CAX1_ORYSJ). Alignment was performed using ClustalW2 (30). Acidic residues are colored in red. (*C*) $^{45}Ca^{2+}$ transport assay of $YfkE^{5G}$ mutant measured using ISO vesicles. Vesicles treated with (*red* squares) or without (black circles) 1 mM EGTA. Error bars represent SDs from three independent experiments. (*D–F*) Isothermal titration curves of Ca^{2+} into a solution containing $YfkE^{WT}$ (*D*), $YfkE^{5G}$ (*E*), or a synthetic peptide of the YfkE TM5-6 loop (*F*). Data fitting was carried out using the software Origin.

of the labeled $YfkE^{A190C}$ (λ_{ex} = 555 nm) gave rise to an emission peak at 677 nm (Fig. 3*B*). Adding 1 mM of EGTA to the protein solution led to an increase in fluorescence intensity. Conversely, FRET signals were decreased in the presence of 50 μM free Ca^{2+}, suggesting reversible conformational changes within the TM5-6 loop mediated by Ca^{2+} binding/unbinding. Of note, Ca^{2+}-induced fluorescence changes were only observed at low free [Ca^{2+}] (50–100 μM) and are diminished at 1.1 mM (Fig. 3*C*), suggesting that the TM5-6 loop senses low levels of cytosolic Ca^{2+} to specifically trigger protein conformational changes. These conformational changes are highly specific for Ca^{2+} since no fluorescence changes were observed in the presence of other cations including Mg^{2+} and Cd^{2+} (Fig. 3*C*). YfkE has two endogenous cysteine residues (Cys^{34} and Cys^{292}), and both are embedded in the TM helices (*SI Appendix*, Fig. S4*A*). Labeling of the $YfkE^{WT}$ protein yielded weak FRET signals that were irresponsive to Ca^{2+}/EGTA, excluding their involvement in the Ca^{2+}-mediated conformational changes (*SI Appendix*, Fig. S4*B*).

We hypothesized that the conformational changes occurring within the TM5-6 loop are directly mediated by Ca^{2+} binding to the mini-sensor. However, it is also possible that the loop motion results incidentally from Ca^{2+} interaction in the translocation pathway. To rule out this possibility, we found that FRET signals of $YfkE^{A190C}$ were quickly reduced by 40% when free [Ca^{2+}] was increased to 20 μM; the signal was then gradually elevated back to the Ca^{2+}-free signal levels (Fig. 3*D*). However, this U-shaped

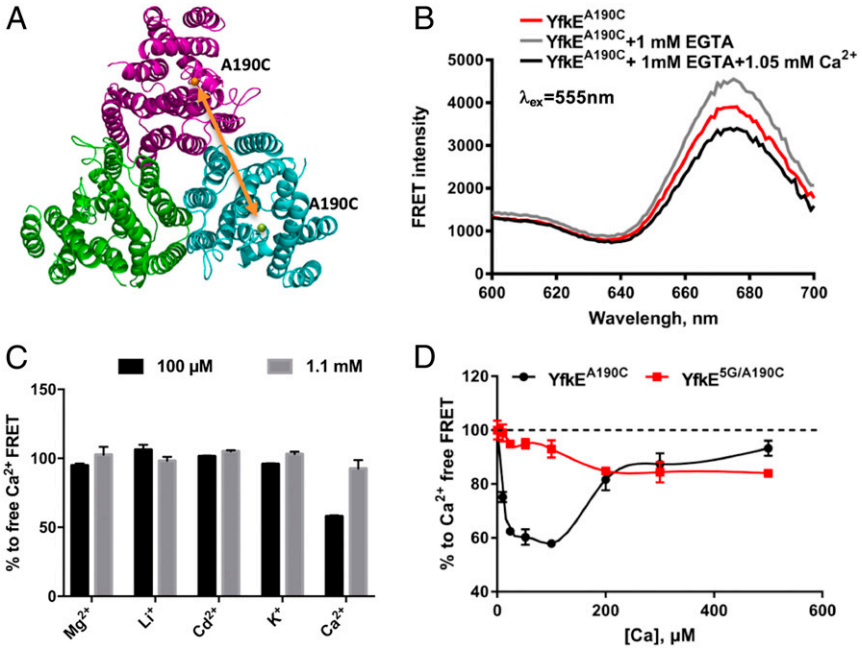

Fig. 3. Conformational changes mediated by the Ca^{2+} mini-sensor. (*A*) Theme of FRET experimental design. The structure of trimeric YfkE was depicted as a cartoon with three protomers colored in red, blue, or green, respectively. FRET signals were measured between two A190 positions from adjacent protomers as indicated with an orange arrow. (*B*) Fluorescence spectra (λ_{ex}: 555 nm) of Alaxa-labeled $YfkE^{A190C}$ protein (red), added with 1 mM EGTA (gray), and then 50 μM of free Ca^{2+}. (*C*) Changes in fluorescence intensity (%) by adding cations into Ca^{2+}-free $YfkE^{A190C}$ samples ($\lambda_{ex}/\lambda_{em}$: 555/677 nm). (*D*) Changes in fluorescence intensity (%) of labeled $YfkE^{A190C}$ and $YfkE^{5G/A190C}$ proteins as a function of [Ca^{2+}]. Error bars represent SDs.

pattern was completely eliminated by the acidic-motif mutations. Fluorescence intensity of $YfkE^{5G/A190C}$ only slightly declined upon [Ca^{2+}] increase to 500 μM (Fig. 3*D*). Given the fact that $YfkE^{5G}$ maintains an active translocation pathway (Fig. 2*B*), the fluorescence changes observed in $YfkE^{A190C}$ may reflect specific conformational changes in the TM5-6 loop induced by Ca^{2+} binding to the mini-sensor.

To regulate YfkE transport, Ca^{2+}-binding signals generated at the mini-sensor have to be transduced toward the Ca^{2+} translocation pathway. The apo structure of YfkE was crystallized at low pH conditions in which the TM5-6 loop is entirely disordered (12). To gain structural insights into the mechanism of Ca^{2+} regulation, we used MD simulation to study Ca^{2+} binding to YfkE. The missing TM5-6 loop was rebuilt as a random peptide based on the secondary structure prediction (Fig. 4*A*). A YfkE protomer was reconstituted in a lipid bilayer composed of 70% phosphatidylethanolamine and 30% phosphatidylglycerol (*SI Appendix*, Fig. S5). The simulation was performed in the presence of Ca^{2+} for 100 ns (see Movie S1 in the *SI Appendix*). In the simulation, only modest conformational changes were observed within the TM helices (rmsd of <2 Å) (Fig. 4*A* and *SI Appendix*, Fig. S6*A*). In contrast, large conformational changes occurred in the TM5-6 loop region with a rms fluctuation >10 Å (*SI Appendix*, Fig. S6*B*); i.e., the loop moved toward the Ca^{2+} translocation pathway in the first 20 ns, and then it bent over to form a hairpin-like structure (Fig. 4*A*). These conformational changes were apparently induced by Ca^{2+} binding to the loop. Two acidic-motif residues Glu^{196} and Glu^{198} and Gln^{186} form a Ca^{2+}-binding site to coordinate one Ca^{2+} ion, stabilizing the hairpin structure (Fig. 4*B*). These stimulation results are in line with our FRET analysis (Fig. 3 *B–D*) and support the hypothesis that Ca^{2+} binding to the mini-sensor induces large conformational changes within the TM5-6 loop.

One of the most interesting structural changes we observed is within an upstream fragment adjacent to the acidic motif. Formation of the Ca^{2+}-binding-mediated hairpin structure pushed an upstream fragment toward the Ca^{2+} translocation pathway (Fig. 4*A*). This upstream fragment is composed of six amino acid residues (LVTHRG) (Fig. 2*A*) and lies on the entry of the intracellular cavity in a zigzag conformation, creating a structural constraint for the Ca^{2+} translocation pathway (Fig. 4*B*). We named this fragment the XIP due to its analogous position to NCX1-XIP previously identified in mammalian NCX1 (20). In the cavity, the XIP interacts with TMs 1 and 2a directly. This interaction led to unwinding and modest kink rotation of TM2a (Fig. 4*C*), accompanied by a rearrangement in the transport Ca^{2+}-binding site. Glu^{72} and Glu^{255} are two essential residues in the transport Ca^{2+}-binding site of YfkE (12). In the apo structure (time = 0), the side chain of Glu^{255} from TM7 interacts with the main chain of the kinked TM2 to lock the translocation pathway. In the simulation, the two kinked helices TMs 2 and 7 moved apart by a distance of 3.5 Å to unlock the pathway, which also enabled the side chains of Glu^{72} to flip toward the transport Ca^{2+}-binding site (Fig. 4*D*). These structural changes suggest that Ca^{2+} binding to the mini-sensor alters the conformation of the pathway-forming helices via intramolecular interactions with YfkE-XIP. It is noteworthy that these conformational changes are clearly induced by Ca^{2+} binding. A control simulation without Ca^{2+} showed that the entire TM5-6 loop including the acidic-motif and XIP regions remained random and disordered (see Movie S2 in the *SI Appendix*).

To gain evidence for the intramolecular interactions between the XIP and the Ca^{2+} translocation pathway, we measured YfkE transport in the presence of a synthetic peptide of the XIP based on the assumption that a homologous peptide would compete with the endogenous XIP segment. ISO vesicles were incubated with the XIP peptide (5 μM) for 10 min prior to transport assays. In accordance with the hypothesis, we found that the Ca^{2+} transport activity of $YfkE^{WT}$ was inhibited by 40% (Fig. 5*A*). In contrast, no inhibition was observed in the presence of a synthetic peptide of the acidic motif (EEEEEPE) measured under the same conditions (Fig. 5*A*). Titration of the XIP peptide revealed a concentration that inhibits response by 50% (IC_{50}) of ~150 nM, suggesting a strong

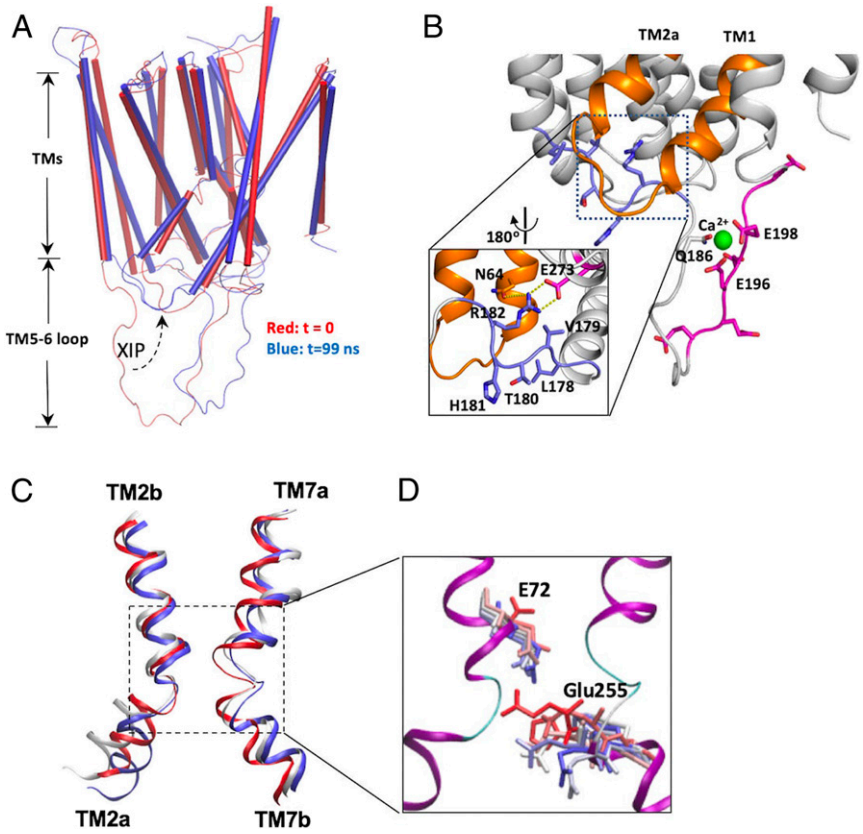

Fig. 4. MD simulation of YfkE shows Ca^{2+}-mediated conformational changes within the TM5-6 loop. (*A*) Superimposition of YfkE snapshots at time t = 0 (red) and t = 99 ns (blue); (*B*) Conformation of the TM5-6 loop (t = 99 ns) showing one Ca^{2+} (green sphere) coordinated by the residues from the acidic motif (red sticks). The XIP region is highlighted using dashed lines and its interactions in the intracellular cavitiy are demonstrated in the inner panel (black square). The XIP (blue sticks) is stabilized in the intracellular cavity by H-bond interactions (yellow dashed lines) between Arg^{182} and other residues (red sticks) and is interacted with TMs 1 and 2a (gold). (*C*) Superimposition of TMs 2 and 7 for snapshots from the trajectory taken at t = 0 (red), 50 (white), and 99 ns (blue); the region of the transport Ca^{2+} site is highlighted using dashed lines and is further demonstrated in detail in *D*. (*D*) superimposition of residues Glu^{72} and Glu^{255} in MD snapshots colored from red (0 ns) through blue (99 ns).

interaction between the XIP and the YfkE (Fig. 5*B*). The inhibitory mode of the XIP was determined by kinetic assays (Fig. 5*B*). As shown in the Eadie–Hofstee plots (Fig. 5*B*, inner panel), the presence of the XIP peptide only reduced V_{max} ($V_m^L = 19.7 \pm 0.4$, $V_{max}^H = 9.1 \pm 0.4$ μmol/min/mg) but had no effect on K_m ($K_m^H = 7.3 \pm 1.8$ μM, $K_m^L = 190.3 \pm 11.3$μM), revealing that the XIP peptide is a noncompetitive inhibitor. Therefore, it is unlikely that the XIP peptide blocks the transporter Ca^{2+}-binding site. Instead, the XIP may alter the conformation of the Ca^{2+} translocation pathway to attenuate the transport activity of YfkE. It is noteworthy that the XIP inhibition resulted in no changes in the biphasic kinetics of YfkE, and similar reductions of V_{max} were seen in both kinetic states (Fig. 5*B*), excluding the possibility that the XIP peptide interferes with the Ca^{2+} mini-sensor.

In the simulation, the residue Arg^{182} plays an important role in stabilizing the XIP segment in the cavity by forming a salt bridge with Glu^{273} from TM7 and an H bond with Gln^{64} from TM1 (Fig. 4*B*). To gain further evidence for this intramolecular interaction, the XIP peptide was treated with phenylglyoxal. Phenylglyoxal reacts specifically with the guanidinium group of Arg^{182} to form a cyclic moiety on the peptide (Fig. 5*C*) (21). This chemical modification completely abolished XIP-mediated inhibition, and no changes in the YfkE activity were found in the presence of the glyoxalated XIP peptide (Fig. 5*D*). These lines of evidence lend support to the notion that the XIP peptide interacts with YfkE in a similar conformation to that of endogenous XIP as demonstrated in the simulation. The specificity of the XIP was further tested using a synthetic peptide LVTARG where the XIP residue His^{181} that is conserved in the CAX protein family (Fig. 2*C*) is mutated to Ala. The mutation abolished the XIP inhibition (*SI Appendix*, Fig. S7), indicating that a specific structural conformation of the XIP is required to interact with the transporter.

If endogenous XIP occupies the intracellular cavity (Fig. 4*B*), it may prevent the exogenous XIP peptide from accessing this position. In the simulation, positioning the XIP into the cavity is coupled with Ca^{2+} binding to the mini-sensor. Consistent with this prediction, the XIP peptide inhibited YfkE only when ISO vesicles were treated with EGTA to eliminate Ca^{2+} on the intracellular surface, whereas no inhibition was observed when Ca^{2+} was present (Fig. 5*D*). To further demonstrate the role of Ca^{2+} in endo vs. exo XIP competition, we monitored Ca^{2+}-mediated conformational changes in response to the XIP peptide using FRET. In the absence of the XIP peptide, Ca^{2+} binding to $YfkE^{A190C}$ (100 μM of free [Ca^{2+}]) led to a decrease in FRET signals (Fig. 3*D*). However, we found that FRET signals induced by the same levels of Ca^{2+} were increased by 25% in the presence of the XIP peptide (Fig. 5*E*). Titration of the XIP peptide yielded a half maximum at ∼100 nM (Fig. 5*E*), consistent with the IC_{50} obtained in the transport assays (Fig. 5*B*). These results suggest that the XIP peptide alters Ca^{2+}-induced conformational changes within the TM5-6 loop. In line with the transport assays, the effect of the XIP peptide was only observed in Ca^{2+}-free conditions. In the presence of Ca^{2+}, adding the XIP peptide has no effect on the fluorescence signals (Fig. 5*E*). Taken

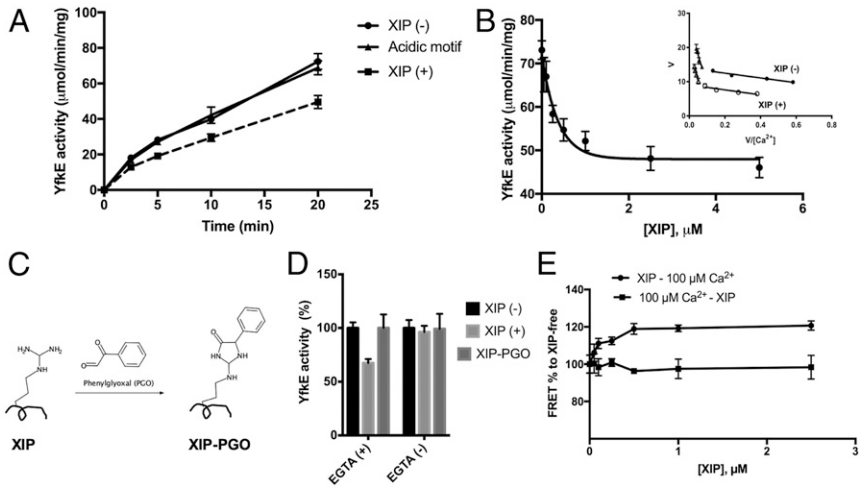

Fig. 5. Identification of the autoinhibitory peptide XIP. (*A*) Time course of the Ca^{2+} transport assay of $YfkE^{WT}$ measured using ISO vesicles pretreated with 1 mM EGTA in the presence of 5 μM synthetic peptide of the XIP or its acidic motif. (*B*) YfkE activity as a function of [XIP] using vesicles treated with 1 mM EGTA. Data fitting into single exponential decay using the software Graphpad Prism 7. (*C*) Theme of the XIP modification by phenylglyoxal. (*D*) Ca^{2+} transport activity of $YfkE^{WT}$ measured with vesicles (20 min) treated with (+) or without (–) EGTA in the presence of 5 μM XIP or modified peptide XIP-dicarbonyl phenylgyoxal (PGO). (*E*) Fluorescence ($\lambda_{ex}/\lambda_{em}$: 555/677 nm) changes (%) of labeled $YfkE^{A190C}$ protein as a function of [XIP]. The XIP peptide was added before (circles) or after adding 100 μM Ca^{2+} (squares). Error bars represent SDs from three independent experiments.

together, these observations support the hypothesis that Ca^{2+} binding to the mini-sensor moves the endogenous XIP segment into the intracellular cavity to prevent exogenous XIP peptide interaction.

Discussion

Elevating cytosolic [Ca^{2+}] is thought to be a primitive and universal cellular response to many developmental cues and environmental challenges. Similar to mammalian cells, plants and prokaryotic cells also maintain tight control of cytosolic Ca^{2+} (typically, submicromolar levels at the resting state) since prolonging an increase in cytosolic [Ca^{2+}] is lethal (8). CAX removes cytosolic Ca^{2+}, facilitating proper Ca^{2+} signaling and normal cellular metabolism. To provoke the appropriate physiological response, the Ca^{2+} signature elicited by each individual stimulus is unique, e.g., in plants, mechanical force, salinity, or osmotic stress shock induce markedly different $[Ca^{2+}]_{cyto}$ perturbations, manifest not only in subcellular locations, but also in the kinetics or magnitude (22–24). A transient increase in Ca^{2+} can be a single spike, biphasic, or as multiple oscillations (8). The great variability and dynamics of Ca^{2+} perturbations necessitate CAX to perform effective Ca^{2+} efflux under varied conditions.

In this study, we reveal a regulatory mechanism for CAX. We found that YfkE senses cytosolic Ca^{2+} levels to adjust its Ca^{2+} transport activity accordingly. This regulatory mechanism is governed by a type of intracellular Ca^{2+} mini-sensor with a micromolar Ca^{2+}-binding affinity located within the TM5-6 loop (Fig. 2*F*). When the cytosolic [Ca^{2+}] is high, Ca^{2+} binding to the mini-sensor stabilizes YfkE in a low-affinity mode in order to reach a high transport rate (Fig. 1). By this means, cytosolic [Ca^{2+}] can be rapidly reduced to avert apoptosis and other cytotoxic effects. When cytosolic [Ca^{2+}] decreases, Ca^{2+} release from the mini-sensor switches the transporter to the high-affinity (25× increase) and low-flux mode to further reduce $[Ca^{2+}]_{cyto}$ to the resting levels (Fig. 1). This state transition is also demonstrated in the biphasic FRET changes in $YfkE^{WT}$. As shown in Fig. 3*D*, the FRET signals were quickly reduced at the low Ca^{2+} levels. The half maximum of this phase is at ∼10 μM, consistent with the K_d (4.7 ± 0.9 μM) of the TM5-6 loop measured by ITC (Fig. 2*F*), suggesting conformational changes mediated by Ca^{2+} binding to the mini-sensor. Upon further [Ca^{2+}] increase, the FRET signals slowly returned back to the Ca-free level (Fig. 3*D*). This second phase may represent Ca^{2+} binding to the transport site since its half maximum at ∼170 μM matches well with the K_m^L (175.2 ± 38.2 μM) of the low-affinity state of YfkE (Fig. 1). These data lend further support to our hypothesis that YfkE is stabilized at the low-affinity transport state at the high Ca^{2+} levels in the cell. That cooperativity between the transport Ca^{2+}-binding site and the mini-sensor is important to achieve the state transition is supported by several lines of evidence. For example, the 5G mutation did not lock the transporter at the high-affinity transport state, instead, it impaired the transport Ca^{2+}-binding affinity and completely abrogated the transition (Fig. 2*C*). This highly cooperative substrate self-regulation may enable YfkE to seamlessly fulfill its Ca^{2+} clearance role within a broad range of $[Ca^{2+}]_{cyto}$ perturbations.

Our FRET measurements suggest that a large conformational change within the TM5-6 loop is induced by Ca^{2+} binding to the mini-sensor (Fig. 3). Based on the simulation, Ca^{2+} binding may mediate local restructuring of the loop (Fig. 4*A*). In the absence of Ca^{2+}, the loop remains unstructured (Movie S2), consistent with the apo structure of YfkE in which the loop is entirely disordered (12). In the unstructured condition, the transporter is kept in a high-affinity state as shown by kinetic assays (Fig. 1). Therefore, the apo structure of YfkE may represent the high-affinity Ca^{2+} transport state (Fig. 6 *A* and *B*). In the YfkE structure, several polar residues important for Ca^{2+} transport, including Asn^{69}, Asn^{99}, Glu^{255}, and Asn^{252}, are tightly packed at the kink interaction of TMs 2 and 7, which assembles a high-affinity Ca^{2+}-binding site in the midpathway (Fig. 6 *C* and *D*).

In the presence of Ca^{2+}, the mini-sensor region forms an antiparallel hairpin structure, concurrently moving the adjacent XIP segment into the intracellular cavity to stabilize TMs 1 and 2a (Fig. 4*B*). This intramolecular interaction was evidenced by specific inhibition of YfkE by a synthetic peptide of the XIP (Fig. 5*A*). Although how the XIP peptide inhibits YfkE is still an interesting question, it is anticipated that the XIP peptide interacts in the intracellular cavity in a similar conformation to that of the endogenous XIP segment based on the facts that 1) the inhibition exhibits a noncompetitive behavior (Fig. 5*B*); 2) neutralization of Arg^{182} abrogates the inhibition (Fig. 5*D*); and 3) the XIP peptide interrupts conformational changes mediated by the mini-sensor (Fig. 5*E*). In all of our assay methods, peptide

interaction took place only in Ca^{2+}-free conditions (Fig. 5 *D* and *E*), strongly implying an interplay between the XIP segment and the Ca^{2+} mini-sensor.

Although the structures of YfkE and VCX1 share a high structural similarity (Fig. 6 *A* and *B*), the TM5-6 loop is well resolved in the Ca^{2+}-bound structure of yeast VCX1 (13). In the VCX1 structure, the TM5-6 loop forms an α-helix laying across the entry of the intracellular cavity (Fig. 6*B*) in a similar pose to that found in our YfkE MD simulation (Fig. 4*B*). This conformation is stabilized by interactions between the TM5-6 helix and the TM helices inside the translocation pathway. Two acidic-motif residues Glu^{230} and Asp^{234} and two carboxylate residues (Glu^{83} and Asp^{87}) from TM1 form a Ca^{2+}-binding site to coordinate two Ca^{2+} ions in the intracellular cavity (*SI Appendix*, Fig. S8). Positioning of the TM5-6 helix in the cavity appears to push TMs 1, 2a, and 6 away from others on the intracellular surface (Fig. 6*B*). TM2a and 7b are separated by a long distance of 14 Å measured at their kink interaction compared to 6 Å in YfkE, while their extracellular halves TM2b and 7a are still well superimposed between the two structures (Fig. 6*C*). YfkE and VCX1 have identical residues at the transport Ca^{2+}-binding site. In contrast to the tightly packed substrate-binding site in YfkE (Fig. 6*D*), the transport Ca^{2+}-binding site of VCX1 appears to be loose, and three water molecules are also involved in Ca^{2+} coordination (Fig. 6*E*). These structural differences are consistent with the YfkE simulation data (Fig. 4 *C* and *D*) and support the hypothesis that the Ca^{2+} mini-sensor regulates YfkE transport by altering the conformation of the transport Ca^{2+}-binding site. Considering the fact that YfkE switches to a low-affinity mode when Ca^{2+} binds to the acidic motif (Fig. 1), we hypothesize that the Ca^{2+}-bound structure of VCX1 represents the conformation of the low-affinity Ca^{2+} transport state (Fig. 6*E*).

Based on our results and structural analysis, a working model for the intracellular Ca^{2+} regulatory mechanism is proposed: YfkE remains in a high-affinity low-flux state when the cytosolic Ca^{2+} level is low (Fig. 7*A*). When $[Ca^{2+}]_{cyto}$ increases, Ca^{2+} binding to the mini-sensor induces allosteric conformational changes within the intracellular loop between TM5 and 6 to push the XIP toward the intracellular cavity (Fig. 7*B*). The movement alters the conformation of the Ca^{2+} translocation pathway by expanding the transport Ca^{2+}-binding site, consequently, converting YfkE to a low-affinity and high-flux state in order to facilitate fast Ca^{2+} efflux across the cell membranes (Fig. 7*C*).

Although the acidic motif is conserved in the CAX family (5), the motifs of carboxylate residues vary noticeably (Fig. 2*C*). *Arabidopsis* CAX1 has nine tandem carboxylate residues within the TM5-6 loop, accounting for 30% of the amino acid sequence. These varied acidic-motif sequences may form different Ca^{2+} sensor conformations; for example, while the TM5-6 loop of YfkE appears to form a hairpin structure (Fig. 4*B*), the loop of VCX1 forms an α-helix (Fig. 6*A*). These acidic-motif sequences could mediate distinct conformational changes in response to Ca^{2+}, which may help to define the specific role of CAX in Ca^{2+} homeostasis in individual cell types. In addition to the acidic motif, the sequence of the XIP is conserved in other CAX proteins (Fig. 2*B*). In the VCX1 structure, the XIP forms the amino terminus of the acidic-motif helix, which is in close proximity to TMs 1 and 2a (Fig. 6*B*), similar to that demonstrated in the YfkE

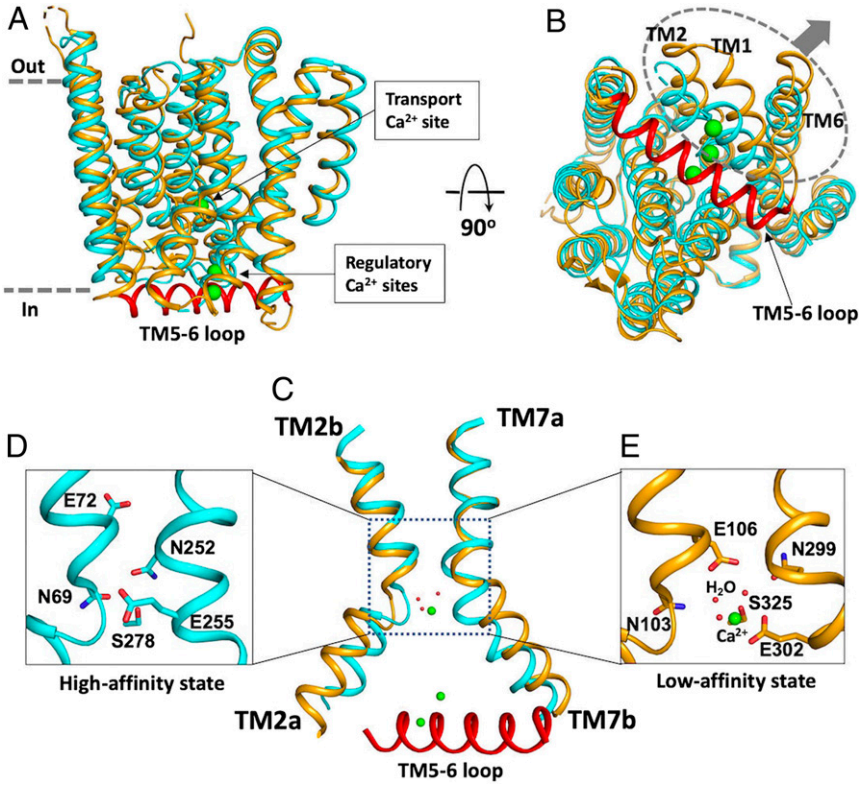

Fig. 6. Comparison between the structures of apo form YfkE and Ca^{2+}-bound VCX1 shows conformational changes mediated by the TM5-6 loop. (*A* and *B*) Superimposition of the structures of YfkE (Protein Data Bank [PDB] code: 4KJS, colored in cyan) and VCX1 (PDB code: 4K1C, colored in yellow) viewed in the membrane (*A*) or from the cytoplasmic side (*B*). In VCX1, the helix of the TM5-6 loop was stabilized by Ca^{2+} ions (green spheres) on the cytoplasmic membrane surface. A N-terminal fragment (amino acid residues 22–40) was removed from VCX1 for clarity. In *B*, TMs 1, 2, and 6 moving away from the TM5-6 helix are highlighted in a dashed circle and indicated with arrows. (*C*) Superimposition of TMs 2 and 7 between YfkE and VCX1, showing that positioning of the TM5-6 helix in the intracellular cavity pushes TM2a and 7b away but not TM2b and 7a. (*D* and *E*) Transport Ca^{2+}-binding site of YfkE (*D*) or VCX1 (*E*) formed by the same set of residues (sticks). In VCX1 (*E*), the Ca^{2+}-binding site is enlarged compared to that of YfkE (*D*) with three water molecules (red spheres) involved in Ca^{2+} coordination.

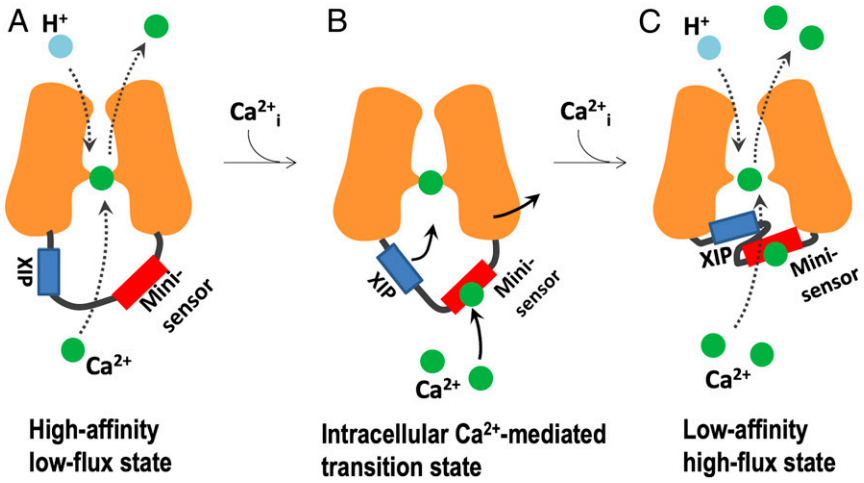

Fig. 7. A working model of the intracellular Ca^{2+} regulatory mechanism of YfkE. (*A*) YfkE remains in a high-affinity low-flux state when the cytosolic [Ca^{2+}] is low. (*B*) Upon increasing cytosolic [Ca^{2+}], Ca^{2+} binding to the mini-sensor induces protein conformational changes within the intracellular loop between TM5 and 6, pushing the XIP toward the intracellular cavity to alter the conformation of the Ca^{2+} translocation pathway, creating a low-affinity high-flux state to facilitate fast Ca^{2+} efflux across the cell membranes (*C*).

simulation (Fig. 4*B*). Therefore, the structures of YfkE and VCX1 serve as a pair of models to study the transport regulatory mechanism of CAX proteins.

Positioning of the TM5-6 loop in the intracellular cavity also raises a question regarding the role of TM2a in the Ca^{2+} transport mechanism. In the previous hypothesis, rotation of TM2a is important in mediating conformational transition from an inward-open to an outward-open state (12). This hypothesis was mainly based on the structural differences between YfkE/VCX1 and NCX_{mj}. However, in both the VCX1 structure and the simulated YfkE, movement of TM2a is restricted by the Ca^{2+}-stabilized TM5-6 loop (Fig. 4*B* and *SI Appendix*, Fig. S8). It is unlikely that folding/unfolding of the TM5-6 loop occurs in each transport cycle since 60% of the YfkE activity still remains in the presence of the XIP synthetic peptide, which appears to block conformational changes in TM2a in a Ca^{2+}-independent manner (Fig. 5 *B* and *D*). Of note, NCX_{mj} lacks an acidic motif (15). Based on our data, rotation of TM2a may not be required for conformational transition of CAX; instead it may serve as a "clutch" to adjust the conformation of the transport Ca^{2+}-binding site.

In this study, we have identified a type of Ca^{2+} mini-sensor and a XIP sequence in the CAX protein family and elucidated their important roles in the Ca^{2+} regulatory mechanism of YfkE. Interestingly, the XIP has also been found in the mammalian cardiac exchanger NCX1 previously (20). Despite the fact that NCX1-XIP has no sequence homology to YfkE-XIP, the two peptides share several similarities: 1) Equivalent locations: NCX1-XIP is located within the large regulatory loop of TM5-6 in a position between TM5 and tandem CBD domains (*SI Appendix*, Fig. S9); 2) similar characteristics of inhibition: a synthetic peptide of NCX1-XIP partially inhibited NCX1 by a maximum of 70% and the inhibition was noncompetitive (20); and 3) the NCX1-XIP peptide interacts with NCX1 on the cytoplasmic surface with a high affinity (20). The sequence of the XIP is critical for NCX1 regulation; i.e., mutation of a single lysine residue within NCX1-XIP abolished Na^+-dependent inactivation and impaired Ca^{2+} regulation of the exchanger (25), suggesting an interplay between the XIP and the adjacent CBD domains within the TM5-6 loop. Furthermore, the XIP also interacts with other signaling molecules, such as calmodulin and phosphatidylinositol 4,5-bisphosphate to regulate NCX1 activity (26). The mechanism identified in YfkE may provide insights to study the regulatory mechanism of mammalian NCX1.

Materials and Methods

$^{45}Ca^{2+}$ transport was measured using ISO vesicles generated from *E. coli* BL21(DE3) cells expressing WT or mutant YfkE as we described previously (12). The YfkE proteins fused with a His tag at the N terminus were expressed in an *E. coli* C41(DE3) strain in autoinduction medium and purified using *n*-dodecyl-β-maltoside as described in our previous structural study (12). The proteins were purified by two steps: Ni-nitrilo-triacetic acid resin followed by size-exclusion chromatography using a Superdex 200 column. For ITC assays, the YfkE proteins were decalcified by adding 10 mM EGTA and then separated using size-exclusion chromatography. ITC assays were performed by titrating Ca^{2+} into a solution of 5 μM protein or peptide on a VP-ITC device (Microcal LLC) as we previously described for CBD1 (27). To perform FRET assays, the YfkE proteins were labeled with Alexa Fluor 555 and 647 (molar ratio = 1:1:2) (Thermo Fisher). FRET assays were carried out with 100 μL protein (5 μM) in a Synergy H1 microplate reader at room temperature. Peptides (>95% purity) were custom synthesized (Biomatik). Peptide modification by phenylglyoxal was carried out using a published protocol (21). MD simulations were performed on a loop-rebuilt YfkE monomer embedded in a palmitoyloleoyl PE/palmitoyloleoyl PG model membrane using the NAMD program (28) and the CHARMM36 force field (29). See details in the *SI Appendix*.

Data Availability. All data relevant to this paper are available in the main text and the *SI Appendix*. Full methods can be found in *SI Appendix, Materials and Methods*.

ACKNOWLEDGMENTS. We thank the Texas Advanced Computing Center (TACC) for a computational resource. This study was supported by National Institutes of Health Grant R01GM097290 and American Heart Association Grant 18TPA34230046 to L.Z., and National Institutes of Health Grant R01GM124233 to A.A.G.

1. M. J. Berridge, M. D. Bootman, H. L. Roderick, Calcium signalling: Dynamics, homeostasis and remodelling. *Nat. Rev. Mol. Cell Biol.* **4**, 517–529 (2003).
2. M. J. Berridge, P. Lipp, M. D. Bootman, The versatility and universality of calcium signalling. *Nat. Rev. Mol. Cell Biol.* **1**, 11–21 (2000).
3. X. Cai, J. Lytton, The cation/Ca^{2+} exchanger superfamily: Phylogenetic analysis and structural implications. *Mol. Biol. Evol.* **21**, 1692–1703 (2004).
4. J. K. Pittman, Vacuolar Ca^{2+} uptake. *Cell Calcium* **50**, 139–146 (2011).
5. T. Shigaki, I. Rees, L. Nakhleh, K. D. Hirschi, Identification of three distinct phylogenetic groups of CAX cation/proton antiporters. *J. Mol. Evol.* **63**, 815–825 (2006).
6. K. D. Hirschi, Expression of Arabidopsis CAX1 in tobacco: Altered calcium homeostasis and increased stress sensitivity. *Plant Cell* **11**, 2113–2122 (1999).
7. J. Zhao, B. J. Barkla, J. Marshall, J. K. Pittman, K. D. Hirschi, The Arabidopsis cax3 mutants display altered salt tolerance, pH sensitivity and reduced plasma membrane H^+-ATPase activity. *Planta* **227**, 659–669 (2008).

8. P. J. White, M. R. Broadley, Calcium in plants. *Ann. Bot.* **92**, 487–511 (2003).
9. M. Fujisawa, Y. Wada, T. Tsuchiya, M. Ito, Characterization of Bacillus subtilis YfkE (ChaA): A calcium-specific Ca^{2+}/H^{+} antiporter of the CaCA family. *Arch. Microbiol.* **191**, 649–657 (2009).
10. D. M. Ivey *et al*., Cloning and characterization of a putative Ca^{2+}/H^{+} antiporter gene from Escherichia coli upon functional complementation of Na^{+}/H^{+} antiporter-deficient strains by the overexpressed gene. *J. Biol. Chem.* **268**, 11296–11303 (1993).
11. D. C. Domínguez, M. Guragain, M. Patrauchan, Calcium binding proteins and calcium signaling in prokaryotes. *Cell Calcium* **57**, 151–165 (2015).
12. M. Wu *et al*., Crystal structure of Ca^{2+}/H^{+} antiporter protein YfkE reveals the mechanisms of Ca^{2+} efflux and its pH regulation. *Proc. Natl. Acad. Sci. U.S.A.* **110**, 11367–11372 (2013).
13. A. B. Waight *et al*., Structural basis for alternating access of a eukaryotic calcium/proton exchanger. *Nature* **499**, 107–110 (2013).
14. T. Nishizawa *et al*., Structural basis for the counter-transport mechanism of a H^{+}/Ca^{2+} exchanger. *Science* **341**, 168–172 (2013).
15. J. Liao *et al*., Structural insight into the ion-exchange mechanism of the sodium/calcium exchanger. *Science* **335**, 686–690 (2012).
16. D. W. Hilgemann, Regulation and deregulation of cardiac Na^{+}-Ca^{2+} exchange in giant excised sarcolemmal membrane patches. *Nature* **344**, 242–245 (1990).
17. G. M. Besserer *et al*., The second Ca^{2+}-binding domain of the Na^{+}/Ca^{2+} exchanger is essential for regulation: crystal structures and mutational analysis. *Proc. Natl. Acad. Sci. U.S.A.* **104**, 18467 (2007).
18. D. A. Nicoll *et al*., The crystal structure of the primary Ca^{2+} sensor of the Na^{+}/Ca^{2+} exchanger reveals a novel Ca^{2+} binding motif. *J. Biol. Chem.* **281**, 21577–21581 (2006).
19. M. Hilge, J. Aelen, G. W. Vuister, Ca2+ regulation in the Na^{+}/Ca^{2+} exchanger involves two markedly different Ca^{2+} sensors. *Mol. Cell* **22**, 15–25 (2006).
20. Z. Li *et al*., Identification of a peptide inhibitor of the cardiac sarcolemmal Na^{+}-Ca^{2+} exchanger. *J. Biol. Chem.* **266**, 1014–1020 (1991).
21. K. Takahashi, The reactions of phenylglyoxal and related reagents with amino acids. *J. Biochem.* **81**, 395–402 (1977).
22. M. R. McAinsh, A. M. Hetherington, Encoding specificity in Ca^{2+} signalling systems. *Trends Plant Sci.* **3**, 32–36 (1998).
23. M. R. McAinsh, C. Brownlee, A. M. Hetherington, Visualizing changes in cytosolic-free Ca^{2+} during the response of stomatal guard cells to abscisic acid. *Plant Cell* **4**, 1113–1122 (1992).
24. M. R. McAinsh, A. Webb, J. E. Taylor, A. M. Hetherington, Stimulus-induced oscillations in guard cell cytosolic free calcium. *Plant Cell* **7**, 1207–1219 (1995).
25. S. Matsuoka, D. A. Nicoll, Z. He, K. D. Philipson, Regulation of cardiac Na^{+}-Ca^{2+} exchanger by the endogenous XIP region. *J. Gen. Physiol.* **109**, 273–286 (1997).
26. Z. He, S. Feng, Q. Tong, D. W. Hilgemann, K. D. Philipson, Interaction of PIP_2 with the XIP region of the cardiac Na/Ca exchanger. *Am. J. Physiol. Cell Physiol.* **278**, C661–C666 (2000).
27. M. Wu, M. Wang, J. Nix, L. V. Hryshko, L. Zheng, Crystal structure of CBD2 from the Drosophila Na^{+}/Ca^{2+} exchanger: Diversity of Ca^{2+} regulation and its alternative splicing modification. *J. Mol. Biol.* **387**, 104–112 (2009).
28. J. C. Phillips *et al*., Scalable molecular dynamics with NAMD. *J. Comput. Chem.* **26**, 1781–1802 (2005).
29. J. B. Klauda, V. Monje, T. Kim, W. Im, Improving the CHARMM force field for polyunsaturated fatty acid chains. *J. Phys. Chem. B* **116**, 9424–9431 (2012).
30. M. A. Larkin *et al*., Clustal W and Clustal X version 2.0. *Bioinformatics* **23**, 2947–2948 (2007).